Check for updates

Towards a Greener and Scalable Synthesis of $Na_2Ti_6O_{13}$ Nanorods and Their Application as Anodes in Batteries for Grid-Level Energy Storage

Dario M. De Carolis,* Dragoljub Vrankovic, Samira A. Kiefer, Enrico Bruder, Michael Thomas Dürrschnabel, Leopoldo Molina-Luna, Magdalena Graczyk-Zajac, and Ralf Riedel

Grid applications require high power density (for frequency regulation, load leveling, and renewable energy integration), achievable by combining multiple batteries in a system without strict high capacity requirements. For these applications however, safety, cost efficiency, and the lifespan of electrode materials are crucial. Titanates, safe and longevous anode materials providing much lower energy density than graphite, are excellent candidates for this application. The innovative molten salt synthesis approach proposed in this work provides exceptionally pure $Na_2Ti_6O_{13}$ nanorods generated at 900–1100 °C in a yield ≥80 wt%. It is fast, cost-efficient, and suitable for industrial upscaling. Electrochemical tests reveal stable performance providing capacities of ≈100 mA h g^{-1} (Li) and 40 mA h g^{-1} (Na). Increasing the synthesis temperature to 1100 °C leads to a capacity decrease, most likely resulting from 1) the morphology/volume change with the synthesis temperature and 2) distortion of the $Na_2Ti_6O_{13}$ tunnel structure indicated by electron energy-loss and Raman spectroscopy. The suitability of pristine $Na_2Ti_6O_{13}$ as the anode for grid-level energy storage systems has been proven a priori, without any performance-boosting treatment, indicating considerable application potential especially due to the high yield and low cost of the synthesis route.

1. Introduction

Alkali and alkali-earth titanates have recently attracted strong interest due to their excellent physical–chemical properties. In particular, sodium titanates ($Na_2O \cdot nTiO_2$) have been extensively investigated for application as photocatalysts[1,2] and anode materials for lithium-[3] and sodium-ion batteries (LIBs and SIBs).[4] Although graphite-based materials are desirable in terms of energy density, the formation of a solid electrolyte interphase (SEI) film and the phenomenon of lithium plating lead to serious safety concerns.[3] The growth of dendrites causes internal short circuits, resulting in rapid aging or even destruction of the battery.[5,6] In this context, high-potential titanium oxide–based anode materials are expected to overcome these problems due to their inherent high chemical compatibility with the electrolyte. Moreover, they are considered

D. M. De Carolis, Dr. D. Vrankovic,[+] S. A. Kiefer, Dr. M. Graczyk-Zajac,[++] Prof. R. Riedel
Dispersive Solids (DF) Division, Materials Science
Technical University of Darmstadt
Otto-Berndt-Straße 3, Darmstadt D-64287, Germany
E-mail: dario.de_carolis@tu-darmstadt.de

The ORCID identification number(s) for the author(s) of this article can be found under https://doi.org/10.1002/ente.202000856.

[+]Present address: Mercedes-Benz AG, Mercedesstraße 120, Stuttgart 70327, Germany
[++]Present address: EnBW Energie Baden-Württemberg AG, Durlacher Allee 93, Karlsruhe 76131, Germany

Dr. E. Bruder
Physical Metallurgy Division, Materials Science
Technical University of Darmstadt
Alarich-Weiss-Straße 2, Darmstadt D-64287, Germany

Dr. M. T. Dürrschnabel
Institute for Applied Materials – Applied Material Physics (IAM-AWP)
Karlsruhe Institute of Technology (KIT)
Hermann-von-Helmholtz-Platz 1, Eggenstein-Leopoldshafen 76344, Germany

Prof. L. Molina-Luna
Advanced Electron Microscopy (AEM) Division, Materials Science
Technical University of Darmstadt
Alarich-Weiss-Straße 2, Darmstadt 64287, Germany

potential high-safety anodes because of their operating voltage range (1.0–2.0 V),[7,8] being thus a plausible candidate for LIBs.

SIBs hold much promise for energy storage applications due to the high abundance and low cost of sodium, combined with its low redox potential of −2.71 V (Na$^+$/Na) versus standard hydrogen electrode, which is only 0.3 V above that of Li$^+$/Li. However, SIBs are less explored than LIBs and research for promising electrode materials is still a fundamental concern, as analogue materials (especially graphite) used for LIBs are far from reproducing or at least narrowing the same performance in SIB assemblies.[9–14] For Na ions the overall thermodynamic balance is unfavorable and sodium forms graphite intercalation compounds to only a very limited extent.[15] Nongraphitic disordered carbons have been intensively explored as potential anodes for sodium reversible storage.[16–18] However, the major drawback related to most disordered carbons is their weak cycling stability, serious capacity fading upon prolonged cycling, and low-potential sodium insertion leading to the risk of dendritic plating. Thus, in particular for the application of grid storage, SIBs need stable and safe negative electrode materials. Na$_2$Ti$_6$O$_{13}$ (NTO) has been shown to be electrochemically active in a lithium cell.[19] In combination with sodium, the reversible capacity of the material is quite low[20] but forms a plateau at around 0.8 V leading to a high-voltage SIB if coupled with an appropriate high-potential cathode material.

Sodium titanates consist of edge- and corner-sharing TiO$_6$ octahedra forming corrugated sheets responsible for the outstanding chemical stability and anomalously high ionic conductivity.[21–23] Moreover, being a zero-strain material, sodium titanates are characterized by high structural stability.[24] Thus, they are promising candidates for SIB anode materials, as they are not synthesized with Li-containing compounds and do not suffer the outgassing behavior due to impurities typical for Li$_4$Ti$_5$O$_{12}$.[25,26]

Different synthesis routes, notably solid-state reaction and hydrothermal[27–34] and sonochemical[35] synthesis, have been applied to tailor the structure and morphology of sodium titanates with the aim of improving their electrochemical performance. NTO was produced by solid-state reaction[36–39] of anatase with Na$_2$CO$_3$.[36–40] Sol–gel synthesis[41,42] and the soft-template method were successfully implemented by Rudola et al.[20] The latter obtained remarkable electrochemical performance at voltages between 3 and 2 V versus Na$^+$/Na. Further improvement was achieved by submitting Na$_2$Ti$_6$O$_{13}$ precursors to prolonged hydration,[27] leading to a larger interlayer in the tunnel structure of NTOs. The coexistence of the layered and the tunnel structure of Na$_2$Ti$_3$O$_7$ and Na$_2$Ti$_6$O$_{13}$, respectively,[30,32] contributes to an improved electrochemical performance.

Molten-salt synthesis (MSS) is a quite simple technique to produce 1D nanostructures.[43] Using a molten salt as reaction medium facilitates dissolution and precipitation, providing an excellent solvent for oxides.[44] Crystallization occurs by reaching supersaturation either by evaporating the solvent[45] or by cooling the whole system. The ratio of the reactant and salt matrix, the heat treatment, and the type of Ti precursor affect the final product.[46–51] Teshima et al.[1,2,52] and Zhen et al.[53] synthesized Na$_2$Ti$_6$O$_{13}$ in NaCl flux, with anatase nanopowder mixed with Na$_2$CO$_3$ as a reactant. He et al.[45] performed the synthesis in

a NaCl–KCl salt mixture containing anatase nanopowder and Na$_2$CO$_3$. Very recently, the formation of sodium titanates was reported by molten salt electrochemical synthesis.[54,55]

Here we report on an efficient and cost-effective approach to synthesize Na$_2$Ti$_6$O$_{13}$ nanorods with an extremely large aspect ratio in a flux of molten Na$_2$SO$_4$. To our knowledge, TiOSO$_4$ as a precursor in combination with molten Na$_2$SO$_4$ has not been published before. Electrochemical tests of Li and Na half-cells confirmed that NTO nanorods are well suited for grid storage application, compensating a theoretical capacity of just 49.5 mA h g^{-1} with high thermal stability, high rate capability, and low synthesis costs.

This work confirms that MSS is a reliable method, to satisfy the high demand of grid storage application. The observed high purity of the final product and the stable capacity of the Na half-cell support the belief that these results are a starting point for improving the material performances further.

2. Results and Discussion

2.1. XRD Analysis of NTO Nanorods

The crystal structure of NTO-X nanorods, where X is the calcination temperature, has been obtained from the X-ray diffraction (XRD) patterns shown in **Figure 1**. Na$_2$Ti$_6$O$_{13}$ is already crystallizing at 900 °C. A treatment at higher temperatures does not lead to the formation of rutile, as reported elsewhere.[20,21,30,37,42,48,52] The differential thermal analysis (DTA) reported in the Supporting Information (see Figure S5, Supporting Information) confirms this result. The XRD patterns fit the ICSD card No. 186996,[56] confirming the monoclinic C2/m space group having a 3D tunnel structure in which the Na ions reside.[56,57] Compared to the ICSD data, the patterns reveal at 48.6° an enhanced intensity of the lattice plane (020), suggesting an enhanced growth along the direction <010> in which the tunnels develop.[48,52]

No commonly accepted view of the growth mechanism of NTO nanorods has been reported in the literature. According to Dominko et al.,[7] the rods grow preferentially along the
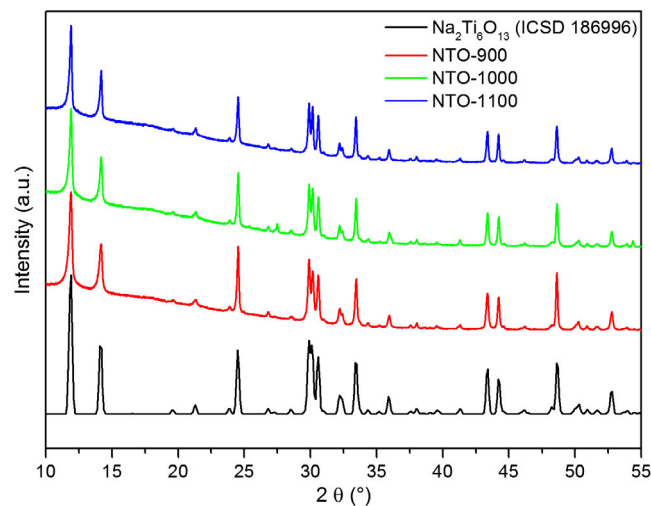

Figure 1. XRD pattern of Na$_2$Ti$_6$O$_{13}$ heat-treated at 900, 1000, and 1100 °C. The data match the ICSD card No. 186996.[56]

ADVANCED
SCIENCE NEWS
www.advancedsciencenews.com

Energy Technology
Generation, Conversion, Storage, Distribution

www.entechnol.de

direction perpendicular and not parallel to the tunnels formed by the edge-sharing octahedra. Pérez-Flores et al.[21] considered <110> as the direction along which the rods develop. Cao et al.[27] identified the facet (−2 0 1) as the most exposed one and as responsible for the Na$^+$ diffusion facilitated through the tunnels. Teshima et al.,[1,2] however, suggested growth along the <010> direction.[1]

Electron backscatter diffraction (EBSD) analysis was performed to determine the growth axis and the most exposed facet. **Figure 2** shows the corresponding EBSD results for a NTO-1100 nanorod (further measurement results of NTO-900 and of a different nanorod in NTO-1100 are reported in the Supporting Information; see Figure S1, Supporting Information). The acquired Kikuchi patterns could be unambiguously indexed, clearly indicating that the growth direction of all analyzed nanorods is parallel to the <010> direction, i.e., the short axis of the unit cell, as visualized in the insert in Figure 2a. The identification of the top facet is not as straightforward, given that the inclination of the surface cannot be identified as precisely as the orientation of the long axis. However, all the analyzed nanorods show crystal orientations indicating a (101) surface plane similar to the example shown in Figure 2a. These results essentially confirm the growth model of Teshima et al.[1]

As a help for the reader, the crystal structure of NTO is shown in **Figure 3**. The three edge-sharing TiO$_6$ octahedra (highlighted with the bright blue) represent the repeating unit composing the tunnels within which two Na ions are placed.

2.2. Morphology of the NTO Nanorods

Figure 4 shows scanning electron microscopy (SEM) micrographs of a sample series heat-treated at different temperatures. The nanorods are organized in cotton wad–like aggregates. Their analysis reveals a considerable difference in the particle dimensions, compared to those of materials obtained by solid-state reaction[36–38,40] or hydrothermal treatment.[28–30,32,33] Hydrothermal treatment and solid-state reaction typically lead to nanorods with a length of only a few microns, whereas MSS produces rods of tenth of microns (maximal length: 40 μm) (reported in Figure S2, Supporting Information). The presence of molten Na$_2$SO$_4$ supports the formation of Na$_2$Ti$_6$O$_{13}$ nanorods
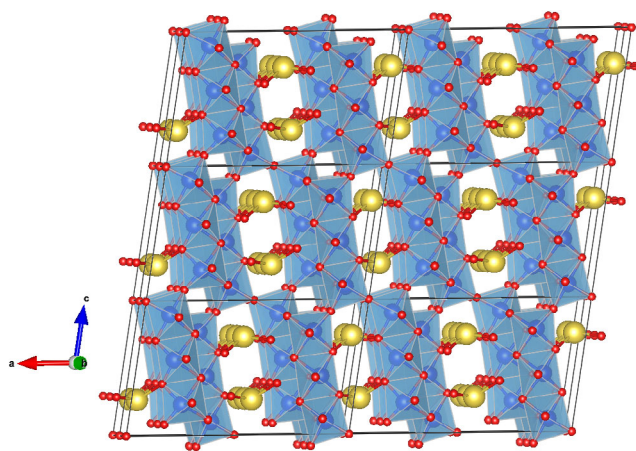

Figure 3. Crystal structure of Na$_2$Ti$_6$O$_{13}$ with the Na$^+$ ions marked in yellow, filling the tunnel structure built up by the TiO$_6$ framework. The red balls represent the oxygen atoms and the blue ones the Ti atoms. The structural model was realized using the 3D visualization software VESTA.[71]

with comparatively smaller diameters by inhibiting the agglomeration of particles along the high-energy surfaces of the crystal. The growth rate is influenced by supersaturation, which in turn is determined by the concentration of the reactants in the salt matrix.[45] Therefore, setting the ratio TiO$_2$:Na$_2$SO$_4$ low enough increases the nucleation rate, limiting the growth rate. The nanorods obtained at 900 °C (see Figure 4, panel a and b) have diameters of ≈150 nm, smaller than those of the samples obtained at 1000 and 1100 °C (≈250 nm). To highlight the effect of the heating temperature on the crystal dimensions, we report in Figure S3, Supporting Information, the diameter difference of the nanorods produced at 900 and 1100 °C at higher magnification. The average length of the rods is higher than 10 μm in all three samples (for clarity low-magnification micrographs are reported in Figure S4, Supporting Information).

The high aspect ratio, compared to that reported in the literature for MSS,[46,48,49] is mainly affected by TiOSO$_4$ as the precursor, having a higher solubility in molten salt than TiO$_2$ nanoparticles.[45,47,52] This leads to an effective dissolution–precipitation process.[58] The supersaturation condition required
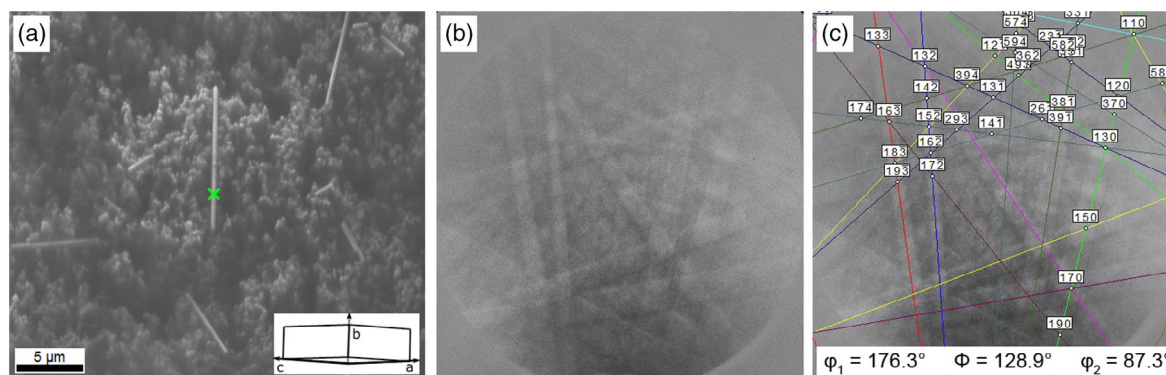

Figure 2. SEM image of NTO-1100 showing nanorods on a carbon pad a) with raw Kikuchi pattern and b) indexed pattern with Euler angles c) acquired at the spot marked by a green cross in (a). The insert in (a) shows the orientation of the unit cell according to the indexed pattern.
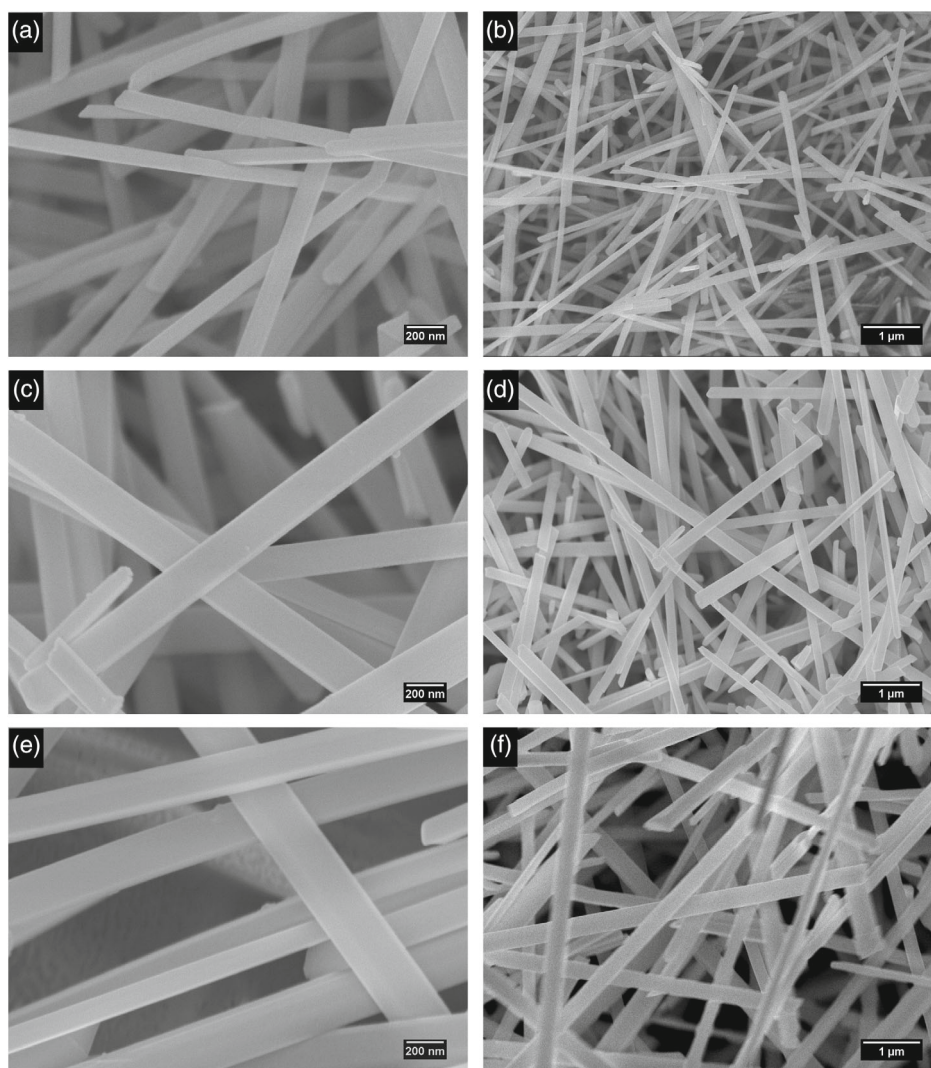
**ADVANCED
SCIENCE NEWS**

www.advancedsciencenews.com

Energy Technology
Generation, Conversion, Storage, Distribution

www.entechnol.de

Figure 4. SEM images of $Na_2Ti_6O_{13}$ obtained at b) 900 °C, d) 1000 °C, and f) 1100 °C, with a,c,e) the respective magnifications.

to initiate the crystal growth is therefore reached at an earlier stage than in the case of TiO_2 as source.

The use of $TiOSO_4$ as precursor, fully immersed in a basic environment constituted by an oxysulfate flux, allows the enhanced growth of long $Na_2Ti_6O_{13}$ nanorods and leads to a highly pure material avoiding the formation of rutile or/and of different sodium titanate structures as described in other works.[20,21,30,31,37,48] In addition, our novel approach leads to high-purity NTO nanorods without posttreatments. Furthermore, their shape is homogeneous (see Figure 4) and no nanoparticles are detected. Raman data (see **Figure 5**) support the high quality of the nanorods.

2.3. Raman and EELS

Figure 5 shows the Raman spectra of the synthesized sodium titanate. In agreement with the DTA results shown in Figure S6, Supporting Information, the Raman data confirm

the remarkable purity of the samples, as typical peaks denoting the presence of rutile (144.5, 241.6, 449.9, and 610.2 cm^{-1}) and anatase (144.5 cm^{-1}) are absent. The presence of sharp peaks with strong intensity evidences the high crystallinity of the samples. Peaks attributable to Na—O band vibrations and Ti—O stretching vibrations are identified at wavenumbers below 400 cm^{-1}.[29] The peaks at 139 and 683 cm^{-1} are attributed to Ti—O—Ti bonds (edge-shared TiO_6 octahedra), scaffolding the tunnel structure.[27,29,59] For these two peaks, we observe a blueshift of ≈ 9 cm^{-1} with respect to the reported literature data.[27] The Ti—O—Ti bonds responsible for the corner-shared TiO_6 are reflected by the vibration band at 750 cm^{-1}. The bands in the range 195–276 cm^{-1}, characteristic of the Na—Ti—O bond,[27] confirm the absence of impurities and good crystallinity in all three samples. Moreover, the lack of a band at 700 cm^{-1}, typically assigned to Ti—O—H vibrations, proves that the samples are fully dehydrated.[29] Finally, the peak located at 876 cm^{-1} is assigned to the short Ti—O stretching vibration with low coordination,[27,29,59–61] indicating that each oxygen atom is bound to at
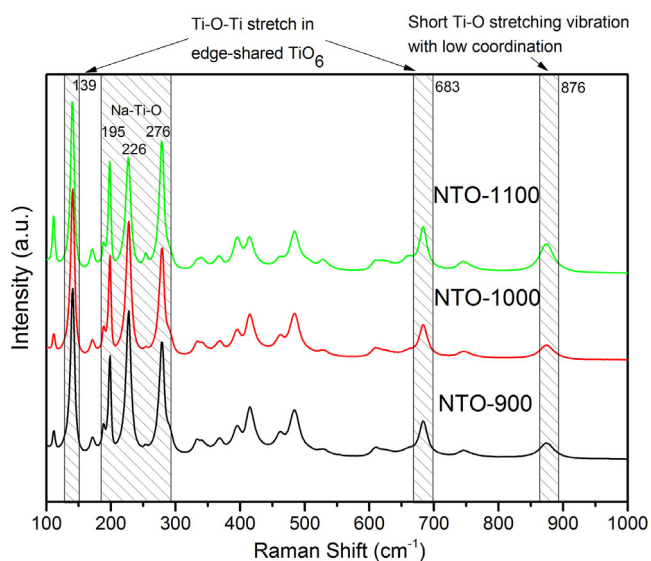
Figure 5. Raman spectra of NTO-900 (black curve), NTO-1000 (red curve), and NTO-1100 (green curve).

least two Ti atoms.[29,40,60] The fact that this peak is increasing by ≈80% with the synthesis temperature suggests a change in the TiO_6 framework structure. In parallel, the band at $226\,cm^{-1}$ is decreasing in intensity (≈20%). For an easier check of these intensity variations, Figure 5 includes a break between 320 and $820\,cm^{-1}$. The decrease of the $226\,cm^{-1}$ band and the increase at $876\,cm^{-1}$ are considered to be due to Ti as well as Na bonds changing simultaneously. The electron energy loss spectroscopy (EELS) measurements presented subsequently provide an additional hint for this finding.

High-resolution transmission electron microscopy (HR-TEM) has been performed on the samples NTO-900 and NTO-1100 to get more insight into the microstructural features. **Figure 6**a shows a bright-field TEM image of NTO-900. The red circle specifies the area being used to acquire the selected area electron diffraction (SAED) pattern shown in Figure 6b. The nanorod is oriented in [0-10] zone-axis orientation and can be indexed using the data of Pérez-Flores et al.[56] Figure 6c is an HR-TEM phase contrast image of the nanorods. Figure 6d is the corresponding fast Fourier transform (FFT) and can—like the diffraction pattern in Figure 6b—be well indexed by the structural data
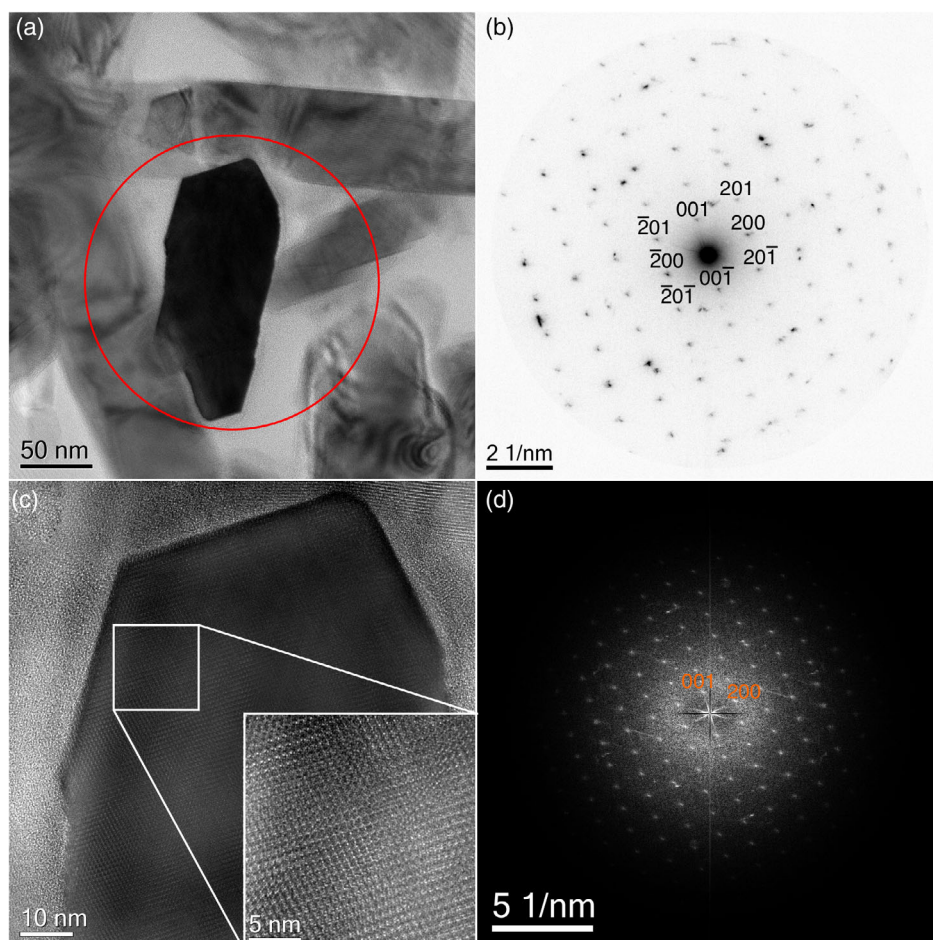

Figure 6. TEM imaging and diffraction in sample NTO-900. a) Bright-field TEM image of an NTO nanorod oriented in [0-10] zone-axis orientation (red circle: SAED aperture) and b) SAED pattern. c) HR-TEM phase contrast image and d) corresponding FFT to (c). The inset in (c) shows a magnified region of (c).

**ADVANCED
SCIENCE NEWS**

www.advancedsciencenews.com

Energy Technology
Generation, Conversion, Storage, Distribution

www.entechnol.de

of Pérez-Flores et al.[56] (see also Figure S7a,b, Supporting Information). **Figure 7**a is a bright-field TEM image of the sample NTO-1100. Figure 7b is the SAED pattern of the region marked by the red circle in Figure 7a. Evidently, the nanorod is oriented along the [001] zone axis of NTO. The high-resolution phase contrast image (Figure 7c) and its corresponding FFT confirm this finding (Figure 7d) (see also Figure S7c,d, Supporting Information). Further information about the local structure was obtained by an atomic resolution scanning transmission electron microscope high-angle annular dark-field (STEM-HAADF)
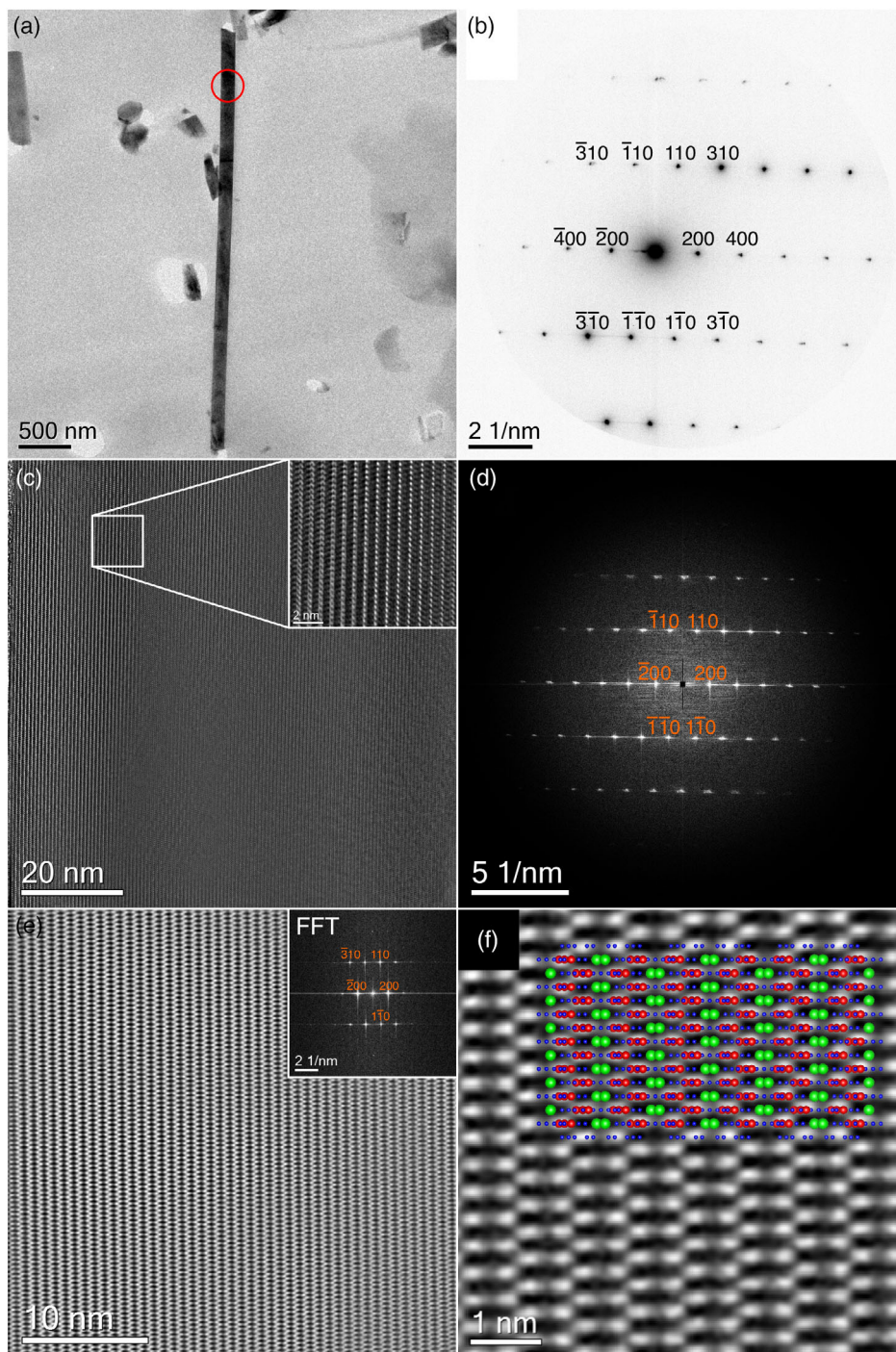

Figure 7. TEM imaging and diffraction in sample NTO-1100. a) Bright-field TEM image of an NTO nanorod oriented in [001] zone-axis orientation (red circle: SAED aperture) and b) SAED pattern. c) HR-TEM phase contrast image and d) corresponding FFT. e) Noise-filtered STEM-HAADF Z-contrast image and f) magnified part of (e) with an atomic model of NTO overlaid (Na: green, Ti: red, O: blue).

Z-contrast image (Figure 7e). The inset in Figure 7e shows the corresponding FFT. Part of Figure 7e is shown as zoomed view in Figure 7f. The titanium-containing atomic columns have a bright contrast due to their larger Z value. Sodium and oxygen are barely recognizable due to the limited spatial resolution and their lower Z value ($Z_{Na} = 11$ and $Z_O = 8$). An atomic model of NTO oriented in [001] zone-axis direction showing Na atoms as green, Ti atoms as red, and O atoms as blue balls has been overlaid for clarity. One immediately recognizes that the bright Ti columns in the STEM-HAADF consist of three Ti columns lying too close to be separated.

Figure 8a shows intensity-normalized low-loss EELS spectra of samples NTO-900 and NTO-1100 embedded in araldite and of anatase and rutile for comparison (Panepinto et al.[62]). The overall electronic structure of both NTO samples is similar to that of rutile or anatase except for the additional Na-$L_{2,3}$ edge present at ≈ 31 eV (see Figure 8b). Furthermore, both samples exhibit a feature located at ≈ 5–8 eV that is similarly present in both rutile and anatase. Launay et al.[63] assigned this feature to the transitions from the top of the valence band into the t_{2g} and e_g levels of the Ti d-orbitals in rutile and anatase. This argumentation should also be valid for NTO. Similarly to rutile and anatase, both NTO samples also show two peaks in the energy region of 10–15 eV. The second one located at ≈ 14 eV in rutile is explained by Launay et al.[63] by special interband transitions originating from specific Ti–O structural units. Further investigations are needed, however, to clearly elucidate the differences in the Ti–O bonding of NTO and TiO_2.

Figure 8c shows core-loss EELS measurements of anatase, rutile, NTO-900, and NTO-1100, respectively. NTO and the two TiO_2 modifications have a number of similarities but also differences in both the Ti-$L_{2,3}$ and the O-K energy loss near edge structures (ELNES). Deconvolution of the EELS spectra shown in Figure 8c displays right above the Ti-$L_{2,3}$ edge onset a slight increase in signal intensity resulting in a difference in the peak-height ratio. This difference is more prominent in NTO-900 than in NTO-1100. In addition, the L_3t_{2g} peak is less prominent in NTO than in both TiO_2 modifications. Furthermore, the L_3e_g peak of both rutile and anatase is asymmetric, whereas it is not in NTO. Monochromated EELS measurements of Cheynet et al.[64] show that this asymmetry is due to a splitting of the L_3e_g peak into two to three single peaks depending on the actual TiO_2 modification. Also, the L_2 edge exhibits some differences that need to be addressed. The L_2e_g peak of the sample NTO-1100 is slightly shifted in energy by ≈ 0.1–0.2 eV to lower energy in comparison to all other Ti-$L_{2,3}$ ELNES peaks in rutile, anatase, and NTO-900. The origin of this shift is unclear at present and needs further clarification.

Figure 8c displays, beside the Ti-$L_{2,3}$ lines, also the O-K ELNES of the two NTO samples and of the rutile and anatase reference. All the samples have four distinct peaks labeled a, b, c, and d between 530 and 545 eV energy-loss. These features were also observed for several mixed-valence titanates, e.g., barium titanate.[65] In addition, nanometric effects might alter the O-K ELNES of our material compared to the bulk material. As shown by Gloter et al.,[66] the O-K ELNES of TiO_2 nanotubes is smeared
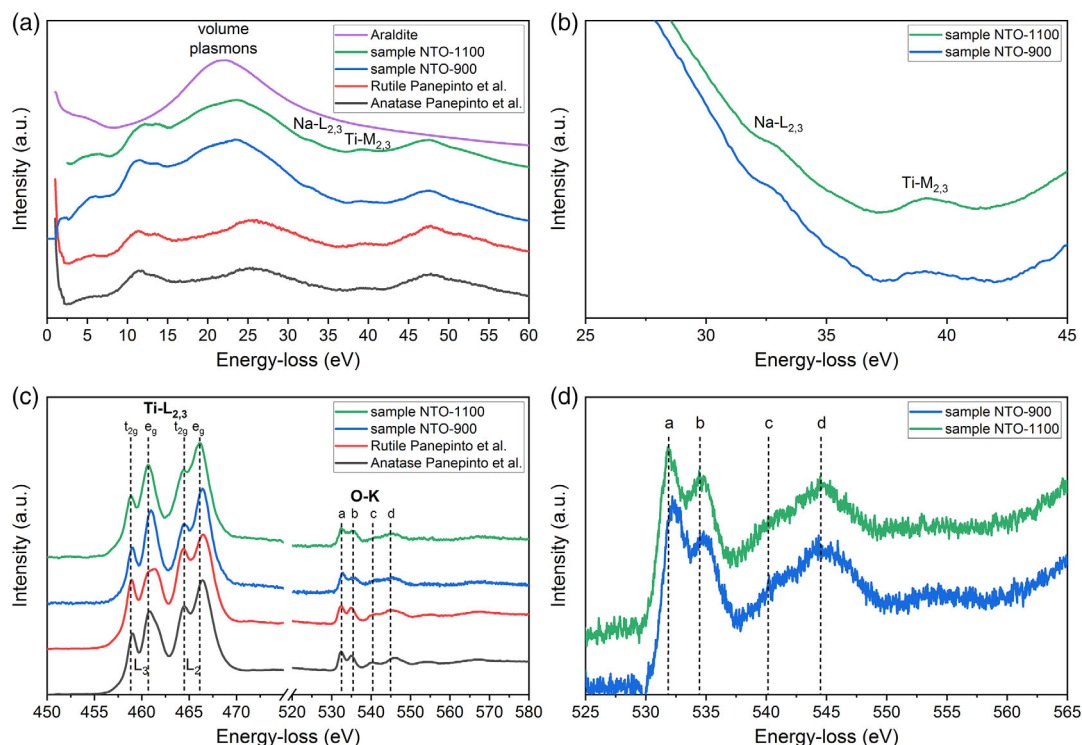

Figure 8. a) Low-loss EELS spectra of rutile,[62] anatase,[62] and samples NTO-900, NTO-1100, and araldite. b) Magnified view of (a) to highlight the Na-$L_{2,3}$ and Ti-$M_{2,3}$ edges for samples NTO-900 and NTO-1100, respectively. c) Ti-$L_{2,3}$ and O-K core-loss EELS spectra of rutile,[62] anatase,[62] and sample NTO-900 and NTO-1100. d) O-K ELNES of sample NTO-900 and NTO-1100, respectively.

**ADVANCED
SCIENCE NEWS**
www.advancedsciencenews.com

Energy Technology
Generation, Conversion, Storage, Distribution
www.entechnol.de

out in the energy-loss range of ≈536–546 eV. Figure 8d shows a magnified view of the O-K ELNES of both NTO samples. As already found for the Ti-L$_{2,3}$ edge, the O-K edge onset for NTO-1100 is shifted by ≈0.2 eV to lower energy compared to that of NTO-900. For the sample NTO-900, the peaks c and d of the O-K ELNES seem to be better separable than for the sample NTO-1100. The relative quantification of NTO-900 and NTO-1100 can be found in the Supporting Information (see Table S2, Supporting Information). These results—together with the changes seen in the Raman spectra (in Figure 5)—lead us to suppose a slight structural modification in the Ti–O sublattice when increasing the synthesis temperature of the NTO sample from 900 to 1100 °C. In agreement with this, recent first-principles calculations[67] propose a low binding energy for twofold coordinated oxygen atoms in the tunnel structure, sitting next to the alkali ion. Their removal is thus energetically most favorable. Therefore, the observed change might be localized in the tunnel region near the alkali ion. However, further studies are needed to corroborate this finding.

2.4. Electrochemical Performance

The electrochemical performance of the NTO nanorods synthesized at 900, 1000, and 1100 °C has been evaluated in a half-cell arrangement by galvanostatic cycling with potential limitation (GCPL) to determine the lithium and sodium storage capacity.

Figure 9a shows the extended cycling performance of the pristine NTO materials sintered at 900, 1000, and 1100 °C for reversible lithium storage. The highest capacities are recovered

by NTO 900, followed by NTO 1000 and NTO 1100. NTO 900 recovers initially 150 mA h g^{-1} and the capacity stabilizes at around 100 mA h g^{-1} for 100 cycles. The coulombic efficiency becomes stable along 100 cycles, being >99% after the first 15 cycles, 28 cycles, and 35 cycles, respectively, for NTO-900, NTO-1000, and NTO-1100. The performance of the half-cell exceeds that reported in the literature (90 mA h g^{-1} at 50 mA g^{-1}[34] and 90 mA h g^{-1} at 12.5 mA g^{-1}[68]). For example, the material synthesized by Li et al.[38] recovers less than 80 mA h g^{-1} at 50 mA g^{-1} after 50 cycles at similar temperatures.

The electrochemical cycling of the NTO in the Na-based cells is shown in Figure 9b. In this case, only a small difference in the electrochemical performance among NTO 900, NTO 1000, and NTO 1100 is found. Initial capacities of ≈45 mA h g^{-1} are recorded, stabilizing at around 40 mA h g^{-1} after 100 cycles. The coulombic efficiency is >98% after around 35 cycles, remaining stable for 100 cycles. These results for a pristine Na$_2$Ti$_6$O$_{13}$ anode present a substantial improvement compared to previous works of Rudola et al.[20] and Cech et al.[30] (both reporting 30 mA h g^{-1} at 49.5 mA g^{-1} for the pure NTO electrode). The latter shows 20 cycles of unstable Na-ion capacity with about similar initial values. Further comparison with literature values from Zhang et al.[29] and Cao et al.[27] is difficult, because of the rather different electrode preparation and cycling conditions.

Figure 9c,d shows the charge (Li$^+$/Na$^+$ insertion) and discharge (Li$^+$/Na$^+$ extraction) profiles for 900, 1000, and 1100 °C samples at a constant current density of 74.4 mA g^{-1}. The electrodes in lithium assembly recover the initial discharge and charge capacities of 245, 256, and 280 mA h g^{-1} with the corresponding first coulombic efficiencies of 60%, 48%, and 38%
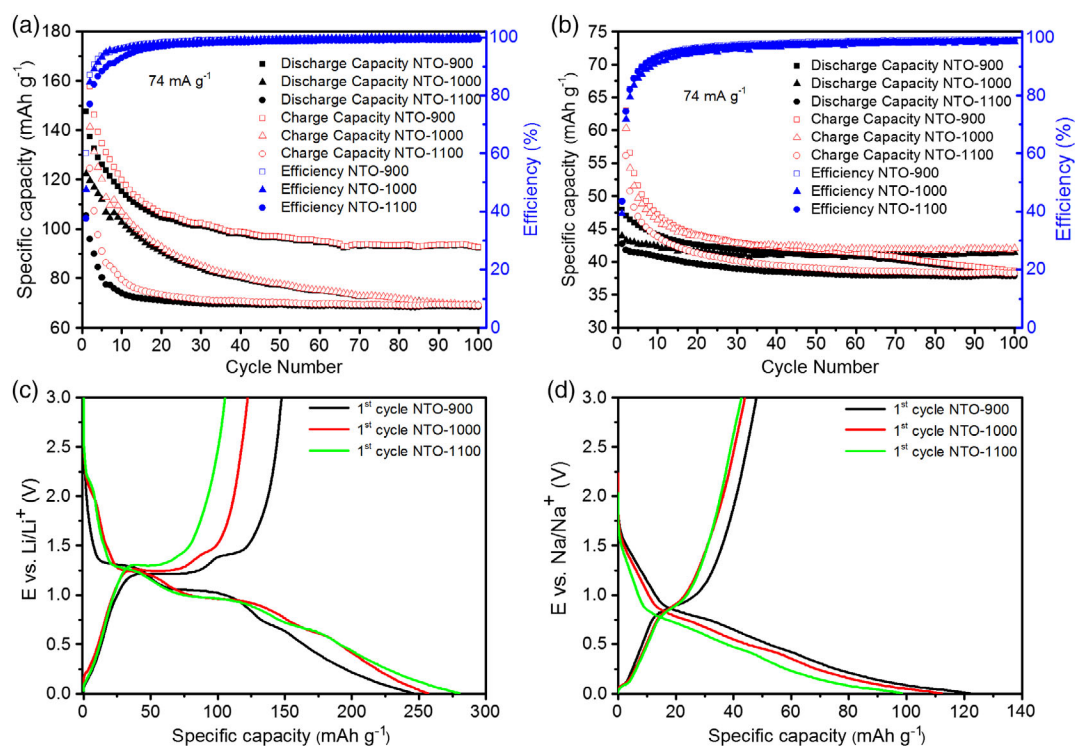

Figure 9. a,b) Charge–discharge capacities of NTO electrodes assessed with 74.4 mA g^{-1} from 0.01 to 3 V versus Li/Li$^+$ and Na/Na$^+$ with their relative efficiencies respectively. c,d) First cycle's charge and discharge profiles of NTO-900, NTO-1000, and NTO-1100 for Li and Na, respectively.

**ADVANCED
SCIENCE NEWS**

www.advancedsciencenews.com

Energy Technology
Generation, Conversion, Storage, Distribution

www.entechnol.de

for NTO-900, NTO-1000, and NTO-1100, respectively. The large irreversible capacities observed over the first cycle can be attributed to 1) the formation of an SEI layer on the nanorods and 2) irreversible intercalation of Li$^+$ ions into $Na_2Ti_6O_{13}$.

In agreement with the literature,[3,21,38,56] reversible lithium insertion produces two plateaus at 1.3 and at 1.0 V and a broad slope at around 0.8 V (Figure 9c). During the Li extraction process, two plateaus appear at 1.2 and 1.4 V for NTO-900 and NTO-1000, whereas for NTO-1100 only the plateau at 1.3 V is recorded. Therefore, the electrochemical insertion of lithium into $Na_2Ti_6O_{13}$ above 0.6 V can be described by $Na_2(Ti^{4+})_6O_{13} + xe^- + xLi^+ \rightarrow Na_2Li_x(Ti^{3+})_6O_{13}$, where the presence of the two plateaus denotes the insertion of lithium ions at two different sites in the tunnel structure.[3,23] The slope from 0.01 to 0.4 V is ascribed to further lithium intercalation into $Na_2Li_xTi_6O_{13}$, which is not reversible.[33]

The electrodes in sodium assembly (Figure 9d) recover the initial discharge and charge capacities of 122, 112, and 98 mA h g^{-1} for NTO-900, NTO-1000, and NTO-1100, respectively, with the corresponding coulombic efficiencies of ≈50–40%. The large irreversible capacities observed over the first cycle are attributed to 1) the formation of an SEI layer on the nanorods due to electrolyte decomposition and 2) intercalation of several Na$^+$ ions into $Na_2Ti_6O_{13}$ at potentials lower than 0.3 V, reaching $Na_6Ti_6O_{13}$ as demonstrated by Shen and Wagemaker.[39] Sodium insertion produces one plateau at 0.8 V, followed by a broad slope (Figure 9d). During the extraction of sodium, one distinct plateau at ≈0.9 V appears for all the investigated materials.[27] Similar to lithium, the electrochemical insertion of sodium into $Na_2Ti_6O_{13}$ above 0.3 V can be described by $Na_2(Ti^{4+})_6O_{13} + xe^- + xNa^+ \rightarrow Na_2Na_x(Ti^{3+})_6O_{13}$, with one distinct plateau signifying the reversible insertion/extraction of one sodium ion. The slope from 0.01 to 0.4 V is due to further irreversible sodium intercalation into $Na_{2+x}Ti_6O_{13}$. There is no significant difference in the insertion/extraction potential versus capacity curves recorded for samples synthesized at different temperatures, whereas a substantial impact of the synthesis temperature on the Li insertion/extraction performance is evident. We rationalize it by the bigger size of the Na ion, leading to a reversible insertion of one sodium ion. In the case of Li, the capacities exceed the theoretical value for one lithium ion (48 mA h g^{-1}). The subtle differences in the microstructure of the materials obtained at lower temperature are responsible for the reversible insertion of at least two lithium ions (96 mA h g^{-1}). According to our findings and recent first-principles calculations,[67] NTO-900 reveals a lower binding energy for twofold coordinated oxygen atoms in the tunnel structure, sitting next to the alkali ion. We suppose that this explains the higher electrochemical performance of the material.

The sample NTO-900 delivers more than 100 and 40 mA h g^{-1} of stable Li and Na storage capacity, respectively. The electrochemical performance is rationalized by the high purity and the elongated rods facilitating the insertion and diffusion of lithium and sodium ions. Further enhancement of the Li storage capacities can be obtained by carbon-coating of the NTO as reported in Liao et al.[33] Nevertheless, this capacity represents more than the half of that of the $Li_4Ti_5O_{12}$ spinel oxide, which is currently the most successful material because of its significant reversible capacity of 175 mA h g^{-1} and its long cycle life.[69]

Taking into account the production cost factors, NTO-900 synthesized using the approach elaborated in this work reports competitive properties in particular for the stationary application where the size/mass of the battery container is not considered a serious obstacle. Moreover, referring to the capacities of graphitic carbons (100 mA h g^{-1} of NTO-900 vs 360 mA h g^{-1} of graphite), one should note the density difference, namely, 3.41 versus 2.2 g cm^{-3}.[70] This leads to a volumetric energy density of around 340 mA h cm^{-3} for NTO-900, which is slightly less than half that of graphite with 790 mA h cm^{-3} (based on nonlithiated graphite), underlining even more the significance of the research on NTO-based anode materials.

The efficiency loss with increasing synthesis temperature is discussed in terms of the change in the active electrode volume arising from the increase in the nanorods' thickness. Second, the efficiency appears to decrease because of changes in the Ti—O bonding and Na bonding inside the tunnel structure. This phenomenon is also supported by the results of the Raman and O-K ELNES studies, as discussed earlier. Further studies are in progress to clarify it.

3. Conclusion

This study reports the molten salt synthesis of $Na_2Ti_6O_{13}$ nanorods, a facile synthesis approach providing a high-purity material in a cost-effective way with no need of additional ad hoc processing. The synthesized nanorods reach an outstanding high aspect ratio (maximum of 400) not yet reported in the literature. Their crystal growth direction was confirmed as <010> via EBSD and HR-TEM investigations. EELS investigations performed to compare the Ti-L$_{2,3}$ and the O-K ELNES of NTO-900 and NTO-1100 show a shift by ≈0.2 eV to lower energy for the sample NTO-1100, indicating a slight change in the Ti—O bonding with increasing synthesis temperature. Raman data confirm this finding.

The electrochemical performance of the $Na_2Ti_6O_{13}$ nanorods is at least comparable with that of the state-of-the-art materials, without the need for additional ad hoc processing. We rationalize the enhanced electrochemical performance of the nanorods in view of their high purity and high aspect ratio. Their unique open tunnel structure facilitates the sodium and lithium transport along the <010> direction in the TiO_6 octahedral framework. The recovered capacities, both in Li-ion and Na-ion half-cells (100 and 40 mA h g^{-1} at 74.4 mA g^{-1} after 100 cycles, respectively), strongly depend on the synthesis temperature. Increasing the synthesis temperature to 1100 °C lowers the capacitances by <20%. This effect is explained by 1) active volume change and 2) alteration in Ti—O bonding and Na bonding inside the tunnel structure.

Only a few insertion electrode materials are reported displaying reversible Na-ion uptake, anode materials in particular being scarce. The MSS in line with the high capacity and the remarkable structural stability of the NTO nanorods qualifies them as promising candidate materials for large-scale energy storage applications in future grid technologies.

4. Experimental Section

Materials Synthesis: The NTO nanorods were obtained through a two-step synthesis: 1) preparation of the precursors by a wet chemical

procedure, followed by 2) heat treatment in molten salt. The following reagents with analytical purity were used for the synthesis: $TiOSO_4$ hydrated (29% Ti, Sigma Aldrich), Na_2SO_4 (anhydrous fine powder), and NaOH solution (32%). A solution of $TiOSO_4$ in deionized water was formed under slow stirring and heating up to 60 °C. The pH was adjusted to $9 < pH < 11$ by titration with 32% NaOH. Na_2SO_4 was added to the solution setting a ratio 1:10 of TiO_2 to salt matrix. The precursor mixture was dried at 110 °C for 24 h and then ground before heat-treating in an alumina crucible under air. The following calcination temperatures were applied: 900, 1000, and 1100 °C, all with 2 h of holding time. The lowest calcination temperature was set to be higher than the melting point of the salt (884 °C). The obtained samples were dissolved in deionized water at 85 °C and filtrated after cooling to room temperature.

Materials Characterization: The phase purity of the samples was ensured by X-ray powder diffraction performed with a HUBER G670-180 Guinier camera (Huber Diffraktiontechnik GmbH & Co. KG, Rimsting, Germany). To identify the growth direction of the nanorods, EBSD was performed using a MIRA3-XMH (TESCAN, Brno, Czech Republic) high-resolution scanning electron microscope, equipped with a DIGIVIEW 5 (EDAX, Mahwah, USA) EBSD system. The nanorods were placed on an adhesive carbon pad and tilted to 70°. Kikuchi patterns were acquired in spot mode with an acceleration voltage of 15 keV on seven different nanorods. The morphological characterization of the samples was carried out via SEM using a JEOL JSM-7600F (Tokyo, Japan) microscope. Raman measurements were performed with a Horiba HR800 micro-Raman spectrometer (Horiba Jobin Yvon, Bensheim, Germany) equipped with a He–Ne laser (633 nm). For each sample, spectra were taken on several different spots to prove the homogeneity of the samples. For TEM, the NTO nanorods were embedded in araldite and subsequently sectioned using an ultramicrotome. TEM characterization was performed in a Thermofisher Talos F200X STEM equipped with four energy-dispersive X-ray (EDX) detectors and a Gatan Enfinium electron energy-loss (EEL) spectrometer with DualEELS capability. The microscope was operated at 200 kV, and the extraction voltage of the field emission electron source was lowered for the EELS measurements from 4050 to 3400 V, resulting in an energy resolution of 0.7–0.8 eV. The convergence and the collection angle for the EELS experiments were 10.5 and 14.1 mrad, respectively. The beam current in the STEM was kept in the range of 100–150 pA as a compromise between beam damage effects and signal intensity. In TEM mode, an objective aperture was always inserted to protect the sample from destruction due to the electron beam.

Electrochemical Characterization: To prepare the working electrodes, the nanorods were mixed with carbon black and a polyvinylidene fluoride binder (85:10:5 wt%) dissolved in *N*-methyl-2-pyrolidone (NMP), forming a slurry. Subsequently, the slurry was applied by a doctor-blading device onto a copper foil and dried for 24 h at 40 °C. Circular electrodes with 10 mm diameter were cut out of the foil and dried for 24 h under vacuum at 80 °C. The film thickness of the tape after drying was around 60 μm, with a loading of active material of ≈ 2 mg cm^{-2}. This is lower than the loadings of commercially used electrodes (graphite 8 mg cm^{-2}), but typically applied in the initial research. Swagelok half-cells were assembled in the argon-filled glove box for the electrochemical tests. The electrodes were tested for two different reference/counter electrodes, elementary sodium and lithium foil, 0.75 mm thick (99.9%, Alfa Aesar). For sodium 180 μL 1 M $NaClO_4$ (mixture of EC:PC:DMC 45:45:1 wt%, homemade) and for lithium 180 μL 1 M $LiPF_6$ (99.9%, mixture of EC:DMC 1:1 wt%, Solvionic) were used as electrolytes. A porous Whatman glass fiber membrane with a diameter of 14 mm served as the separator. Specific capacity values were calculated based on the mass of the active material.

More details about the experimental characterization procedure can be found in the Supporting Information.

Supporting Information

Supporting Information is available from the Wiley Online Library or from the author.

Conflict of Interest

The authors declare no conflict of interest.

[1] K. Teshima, K. Yubuta, T. Shimodaira, T. Suzuki, M. Endo, T. Shishido, S. Oishi, *Cryst. Growth Des.* **2008**, 8, 465.

[2] K. Teshima, S. Lee, S. Murakoshi, S. Suzuki, K. Yubuta, T. Shishido, M. Endo, S. Oishi, *Eur. J. Inorg. Chem.* **2010**, 2010, 2936.

[3] A. Kuhn, J. C. Pérez Flores, M. Hoelzel, C. Baehtz, I. Sobrados, J. Sanz, F. García Alvarado, *J. Mater. Chem. A* **2018**, 6, 443.

[4] Y. Xu, D. Bauer, M. Lübke, T. E. Ashton, Y. Zong, J. A. Darr, *J. Power Sources* **2018**, 408, 28.

[5] N. Williard, W. He, C. Hendricks, M. Pecht, *Energies* **2013**, 6, 4682.

[6] R. V. Bugga, M. C. Smart, *ECS Trans.* **2010**, 25, 241.

[7] R. Dominko, L. Dupont, M. Gaberšček, J. Jamnik, E. Baudrin, *J. Power Sources* **2007**, 174, 1172.

[8] S. Garnier, C. Bohnke, O. Bohnke, J. L. Fourquet, *Solid State Ionics* **1996**, 83, 323.

[9] H. Zhang, I. Hasa, S. Passerini, *Adv. Energy Mater.* **2018**, 8, 1702582.

[10] C. Delmas, *Adv. Energy Mater.* **2018**, 8, 1703137.

[11] Y. Huang, Y. Zheng, X. Li, F. Adams, W. Luo, Y. Huang, L. Hu, *ACS Energy Lett.* **2018**, 3, 1604.

[12] L. Chen, M. Fiore, J. E. Wang, R. Ruffo, D.-K. Kim, G. Longoni, *Adv. Sustainable Syst.* **2018**, 1700153, 37.

[13] T. Liu, Y. Zhang, Z. Jiang, X. Zeng, J. Ji, Z. Li, X. Gao, M. Sun, Z. Lin, M. Ling, J. Zheng, C. Liang, *Energy Environ. Sci.* **2019**, 12, 1512.

[14] J.-Y. Hwang, S.-T. Myung, Y.-K. Sun, *Chem. Soc. Rev.* **2017**, 46, 3529.

[15] J. Sangster, *J. Phase Equilib. Diffus.* **2007**, 28, 571.

[16] D. A. Stevens, J. R. Dahn, *J. Electrochem. Soc.* **2000**, 147, 1271.

[17] S. Wenzel, T. Hara, J. Janek, P. Adelhelm, *Energy Environ. Sci.* **2011**, 4, 3342.

[18] V. Palomares, M. Casas-Cabanas, E. Castillo-Martínez, M. H. Han, T. Rojo, *Energy Environ. Sci.* **2013**, 6, 2312.

[19] R. Dominko, E. Baudrin, P. Umek, D. Arčon, M. Gaberšček, J. Jamnik, *Electrochem. Commun.* **2006**, 8, 673.

**ADVANCED
SCIENCE NEWS**

www.advancedsciencenews.com

Energy Technology
Generation, Conversion, Storage, Distribution

www.entechnol.de

[20] A. Rudola, K. Saravanan, S. Devaraj, H. Gong, P. Balaya, *Chem. Commun.* **2013**, *49*, 7451.

[21] J. C. Pérez-Flores, A. Kuhn, F. García-Alvarado, *J. Power Sources* **2011**, *196*, 1378.

[22] Y. A. Zulueta, P. Geerlings, F. Tielens, M. T. Nguyen, *J. Solid State Chem.* **2019**, *279*, 120930.

[23] C. Ling, R. Zhang, *Phys. Chem. Chem. Phys.* **2017**, *19*, 10036.

[24] I. Hasa, J. Hassoun, S. Passerini, *Nano Res.* **2017**, *3*, 12274.

[25] C. Han, Y. B. He, M. Liu, B. Li, Q. H. Yang, C. P. Wong, F. Kang, *J. Mater. Chem. A* **2017**, *5*, 6368.

[26] T. F. Yi, T. T. Wei, Y. Li, Y. B. He, Z. B. Wang, *Energy Storage Mater.* **2020**, *26*, 165.

[27] K. Cao, L. Jiao, W. K. Pang, H. Liu, T. Zhou, Z. Guo, Y. Wang, H. Yuan, *Small* **2016**, *12*, 2991.

[28] X. Du, H. Yao, M. Ma, T. Feng, B. Zhang, Y. Xu, C. Ma, J. Wang, Y. Huang, *J. Alloys Compd.* **2017**, *721*, 100.

[29] Q. Zhang, T. Zhang, Y. Wei, T. Zhai, H. Li, *J. Mater. Chem. A* **2017**, *5*, 18691.

[30] O. Cech, K. Castkova, L. Chladil, *J. Energy Storage* **2017**, *14*, 391.

[31] Y. Zhang, H. Hou, X. Yang, J. Chen, M. Jing, Z. Wu, X. Jia, X. Ji, *J. Power Sources* **2016**, *305*, 200.

[32] C. Wu, W. Hua, Z. Zhang, B. Zhong, Z. Yang, G. Feng, W. Xiang, Z. Wu, X. Guo, *Adv. Sci.* **2018**, *5*, 1800519.

[33] J.-Y. Liao, T. W. Smith, R. R. Pandey, X. He, C. C. Chusuei, Y. Xing, *RSC Adv.* **2018**, *8*, 8929.

[34] H. Zhang, X. P. Gao, G. R. Li, T. Y. Yan, H. Y. Zhu, *Electrochim. Acta* **2008**, *53*, 7061.

[35] N. G. Fagundes, F. X. Nobre, L. A. L. Basilio, A. D. Melo, B. Bandeira, J. C. C. Sales, J. C. S. Andrade, J. Anglada-Rivera, L. Aguilera, J. Pérez de la Cruz, Y. Leyet, *Solid State Sci.* **2019**, *88*, 63.

[36] C. Wu, Z.-G. Wu, X. Zhang, R. Rajagopalan, B. Zhong, W. Xiang, M. Chen, H. Li, T. Chen, E. Wang, Z. Yang, X. Guo, *ACS Appl. Mater. Interfaces* **2017**, *9*, 43596.

[37] C.-K. Ho, C.-Y. V. Li, K.-Y. Chan, *Ind. Eng. Chem. Res.* **2016**, *55*, 10065.

[38] P. Li, P. Wang, S. Qian, H. Yu, X. Lin, M. Shui, X. Zheng, N. Long, J. Shu, *Electrochim. Acta* **2016**, *187*, 46.

[39] K. Shen, M. Wagemaker, *Inorg. Chem.* **2014**, *53*, 8250.

[40] M. Shirpour, J. Cabana, M. Doeff, *Energy Environ. Sci.* **2013**, *6*, 2538.

[41] H. Y. Wang, J. Y. Liao, B. K. Zou, Z. F. Tang, X. Sun, Z. Y. Wen, C. H. Chen, *Mater. Lett.* **2017**, *186*, 326.

[42] A.-L. Sauvet, S. Baliteau, C. Lopez, P. Fabry, *J. Solid State Chem.* **2004**, *177*, 4508.

[43] M.-A. Einarsrud, T. Grande, *Chem. Soc. Rev.* **2014**, *43*, 2187.

[44] X. Liu, N. Fechler, M. Antonietti, *Chem. Soc. Rev.* **2013**, *42*, 8237.

[45] H. He, W. Yao, C. Wang, X. Feng, X. Lu, *Ind. Eng. Chem. Res.* **2013**, *52*, 15034.

[46] J. Chen, *Ceram. Int.* **2015**, *41*, 9018.

[47] X. Zhou, D. Zhong, H. Luo, J. Pan, D. Zhang, *Appl. Surf. Sci.* **2018**, *427*, 1183.

[48] C.-Y. Xu, J. Wu, P. Zhang, S.-P. Hu, J.-X. Cui, Z.-Q. Wang, Y.-D. Huang, L. Zhen, *CrystEngComm* **2013**, *15*, 3448.

[49] P. Billik, M. Caplovicovà, L. Caplovic, *Mater. Res. Bull.* **2010**, *45*, 621.

[50] P. M. Rørvik, T. Lyngdal, R. Sæterti, A. T. J. Van Helvoort, R. Holmestad, T. Grande, M. A. Einarsrud, *Inorg. Chem.* **2008**, *47*, 3173.

[51] K. H. Yoon, Y. S. Cho, D. H. Kang, *J. Mater. Sci.* **1998**, *33*, 2977.

[52] K. Teshima, S. Sugiura, K. Yubuta, T. Suzuki, M. Endo, T. Shishido, S. Oishi, *J. Ceram. Soc. Jpn.* **2007**, *115*, 230.

[53] L. Zhen, C. Y. Xu, W. S. Wang, C. S. Lao, Q. Kuang, *Appl. Surf. Sci.* **2009**, *255*, 4149.

[54] H. Li, K. Wang, W. Li, S. Cheng, K. Jiang, *J. Mater. Chem. A* **2015**, *3*, 16495.

[55] Y. Chiba, D. Koizumi, M. Saito, T. Motohashi, *CrystEngComm* **2019**, *21*, 3223.

[56] J. C. Pérez-Flores, F. García-Alvarado, M. Hoelzel, I. Sobrados, J. Sanz, A. Kuhn, *Dalt. Trans.* **2012**, *41*, 14633.

[57] S. Andersson, A. D. Wadsley, *Acta Crystallogr.* **1962**, *15*, 194.

[58] T. Kimura, in *Advances in Ceramics – Synthesis and Characterization, Processing and Specific Applications* (Ed: C. Sikalidis), InTech, Rijeka, Croatia **2011**, pp. 75–100.

[59] H. Liu, D. Yang, Z. Zheng, X. Ke, E. Waclawik, H. Zhu, R. L. Frost, *J. Raman Spectrosc.* **2010**, *41*, 1331.

[60] C. E. Bamberger, G. M. Begun, *J. Am. Ceram. Soc.* **1987**, *70*, C-48.

[61] Y. Su, M. Lou Balmer, B. C. Bunker, *J. Phys. Chem. B* **2000**, *104*, 8160.

[62] A. Panepinto, M. Michiels, M. T. Dürrschnabel, L. Molina-Luna, C. Bittencourt, P. A. Cormier, R. Snyders, *ACS Appl. Energy Mater.* **2020**, *3*, 759.

[63] M. Launay, F. Boucher, P. Moreau, *Phys. Rev. B – Condens. Matter Mater. Phys.* **2004**, *69*, 035101.

[64] M. Cheynet, S. Pokrant, S. Irsen, P. Krüger, *Ultramicroscopy* **2010**, *110*, 1046.

[65] T. Höche, P. Olhe, R. Keding, C. Rüssel, P. A. Van Aken, R. Schneider, H.-J. Kleebe, X. Wang, A. J. Jacobson, S. Stemmer, *Philos. Mag.* **2003**, *83*, 165.

[66] A. Gloter, C. Ewels, P. Umek, D. Arcon, C. Colliex, *Phys. Rev. B – Condens. Matter Mater. Phys.* **2009**, *80*, 035413.

[67] J. Kanchanawarin, W. Limphirat, P. Promchana, T. Sooknoi, T. Maluangnont, K. Simalaotao, A. Boonchun, P. Reunchan, S. Limpijumnong, J. T. Thienprasert, *J. Appl. Phys.* **2018**, *124*, 155101.

[68] X. K. Zhang, J. J. Yuan, H. J. Yu, X. R. Zhu, Z. Yin, H. Shen, Y. M. Xie, *J. Alloys Compd.* **2015**, *631*, 171.

[69] H. G. Jung, M. W. Jang, J. Hassoun, Y. K. Sun, B. Scrosati, *Nat. Commun.* **2011**, *2*, 516.

[70] A. Jain, S. P. Ong, G. Hautier, W. Chen, W. D. Richards, S. Dacek, S. Cholia, D. Gunter, D. Skinner, G. Ceder, K. A. Persson, *APL Mater.* **2013**, *1*, 011002.

[71] K. Momma, F. Izumi, *J. Appl. Crystallogr.* **2011**, *44*, 1272.